www.nature.com/scientificreports

scientific reports

OPEN

Geoelectrical evidence of fluid controlling slow and regular earthquakes along a plate interface

Hayato Nakamura[1], Hiroshi Ichihara[1]✉, Tada-nori Goto[2], Tetsuo Matsuno[3], Noriko Tada[4], Manaka Kuroda[1] & Shinya Sato[5]

Understanding the distribution of physical properties around shallow subducting plate interfaces, where both destructive and "slow" earthquakes occur due to rapid and slower fault slips, respectively, presents a major scientific and disaster mitigation challenge. Pore water is a key factor in understanding the different slip mechanisms and their spatial relationships; however, its distribution remains understudied. In this study, based on marine magnetotelluric survey in Hyuga-nada, southwestern Japan, we identified distinct resistive and conductive anomalies along the plate interface. These anomalies correspond to areas of scarce pore fluid and high concentration area of pore fluids sourced from subducting seamounts (Kyushu–Palau Ridge), respectively. The wet area corresponds to the slow slip area, whereas the dry and transition areas correspond to areas of fast fault slip. These findings provide clear observational evidence that pore fluid distribution correlates with fault rupture behavior.

Keywords Plate interface, Seamount, Hyuga-nada, Electrical resistivity, OBEM, Slow earthquakes

The development of dense observation networks has enabled us to discover and investigate various seismic phenomena along plate interfaces, including slow earthquakes, which have longer relaxation times than regular earthquakes[1–5]. Because slow earthquakes may be a trigger of devastating earthquakes[5–7] as well as a mechanism of the release of strain energy along megathrusts[8], understanding how the two types of fault slip are related presents a major scientific and disaster-mitigation challenge[4,5]. The spatial dependency of such seismic activity, which is exhibited both at the plate interface depth and along the strike of the subduction interface[4,7,9,10], suggests that elucidation of the physical properties around plate interfaces is important for improving understanding of fault rupture processes. One major factor causing varying fault behavior may be a heterogeneous pore-water distribution[11–14], because the presence of pore water reduces rock strength[15]. Subducted seamounts and ridges can also play an important role because they affect the water supply to the plate interface as well as its shape[10,16,17].

Electrical resistivity measurement is an essential tool for assessing the fluid distribution at plate interfaces because saline pore fluids significantly affect the bulk rock resistivity[17–23]. For example, along the Hikurangi subduction margin in New Zealand, regions of low electrical resistivity, which imply the presence of fluids released from the subducting slab or subducted sediments, are associated with tremor and the occurrence of slow slip events (SSEs)[20,21]. Additionally, the heterogeneous resistivity distribution along the plate interface is related to inter-plate coupling and the areal strain rate[21–23]. However, the existing resistivity models are mostly based on onshore observations and do not cover the marine region where many plate interface phenomena occur. One study in a marine area across the Hikurangi margin has demonstrated the effect of fluid-filled porous regions in seamounts on seismic activities by two-dimensional resistivity modeling[17], but the deep structure and along-strike heterogeneity have not been characterized.

The Hyuga-nada region, which is situated at the western end of the Nankai Trough where the Philippine Sea Plate is subducting under the Eurasian Plate at a convergence rate of 63–68 mm/year toward N55W[24], is well suited for studying the role of structural heterogeneity in fault ruptures. Various types of slow earthquakes and regular earthquakes have been reported in this region (Fig. 1). Regular earthquakes occurring here include frequent M7 class earthquakes, such as the 1968 Hyuga-nada earthquake (M7.5)[25] and the 2024 Hyuga-nada earthquake (M7.1), which prompted Japanese government to issue a massive earthquake warning. Slow

[1]Graduate School of Environmental Studies, Nagoya University, Nagoya, Japan. [2]Graduate School of Science, University of Hyogo, Himeji, Japan. [3]Kobe Ocean-Bottom Exploration Center, Kobe University, Kobe, Japan. [4]Research Institute for Marine Geodynamics, Japan Agency for Marine-Earth Science and Technology, Yokosuka, Japan. [5]Graduate School of Engineering, Kyoto University, Kyoto, Japan. ✉email: ichihara.hiroshi.i9@f.mail.nagoya-u.ac.jp

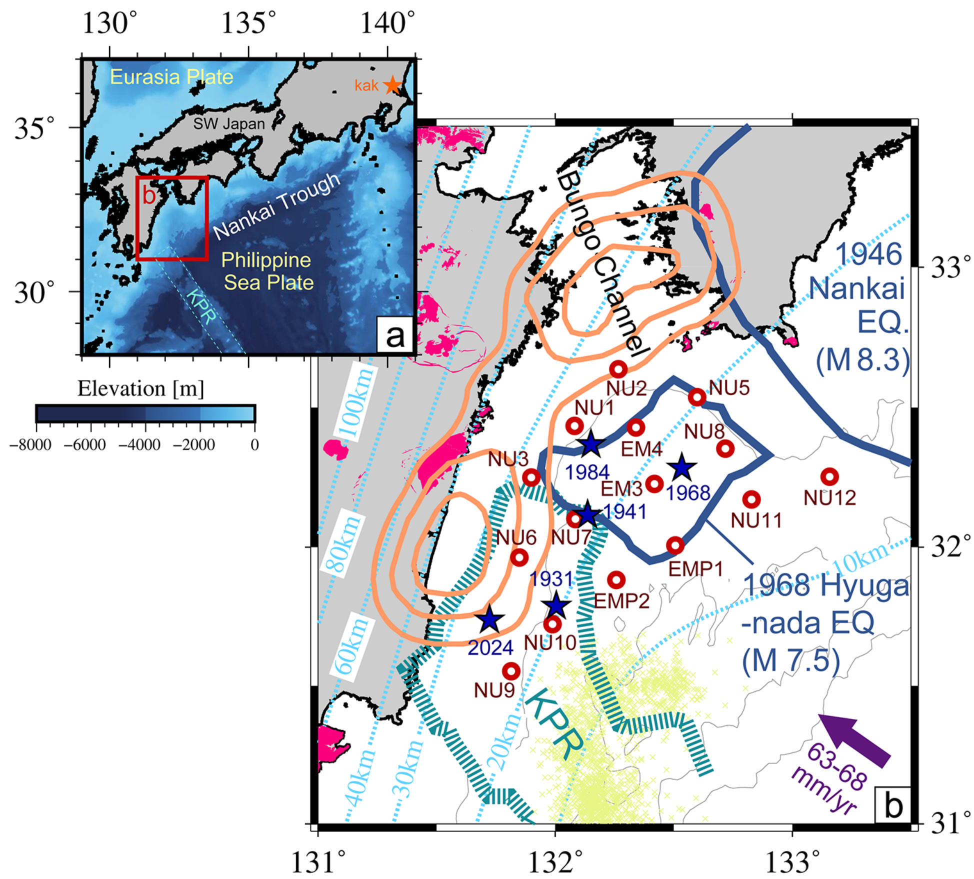

Fig. 1. Study location and bathymetry of the Hyuga-nada region. (**a**) Regional bathymetry. The orange star denotes the Kakioka Geomagnetic Observatory Station of the Japan Meteorological Agency. (**b**) Observation array and fault rupture areas. Red circles denote marine ocean bottom electro-magnetometer observation sites. Sky-blue dotted lines are the depth contours of the plate boundary interface[66]. The turquoise bold dotted line denotes where the Kyushu–Palau Ridge is subducting[29]. Granite areas known from terrestrial geological surveys are shown in magenta[67]. Solid blue lines indicate the slip areas of the 1946 Nankai[68] and the 1968 Hyuga-nada[25] earthquakes. Blue stars denote regular earthquakes (> M7.0) determined by the Japan Meteorological Agency. The orange contours show the total cumulative slip of long-term SSEs (contour interval 20 cm) from 1996 to 2017[27]. The yellow crosses denote the shallow tremors generated from May to July 2013[26]. The purple solid arrow indicates a convergence direction of the Philippine Sea Plate toward the Amurian Plate.

earthquakes, including shallow tremor[26] and SSEs[1,27], have been detected around the regular earthquake (Fig. 1). In addition, the Kyushu–Palau Ridge (KPR), a group of seamounts on the Philippine Sea Plate, is subducting beneath the southwestern part of Hyuga-nada[28]. The slow earthquakes occur near to the subducting seamounts. Areas of low seismic velocity found in the subducted KPR and the overriding plate above the KPR may imply the existence of fluid-filled porous regions that affect the shallow tremors occurring nearby[10,29]. However, because the electrical resistivity distribution in the Hyuga-nada area has not been investigated, direct evidence of the pore-fluid distribution around the plate interface and the subducting KPR has been lacking. The major reason that the resistivity distribution has not been elucidated is the complex oceanic topography, which severely distorts magnetotelluric (MT) impedances and renders conventional 2D analyses impractical[30–33]. For this reason, there have been no previous studies on three-dimensional resistivity structures offshore regions in subduction zone. Recently, however, the analysis of marine MT data using a 3D inversion code based on the finite difference method[34,35] has enabled us to evaluate the subsurface resistivity structure while taking account of the seafloor topography. Therefore, in this study, to elucidated the fluid distribution in the Hyuga-nada area, we conducted marine MT investigations at 15 sites with ocean bottom electro-magnetometers (OBEMs) (Fig. 1). We carefully analyzed MT impedances in the observed marine MT data and obtained the optimum model of electrical resistivity distribution by utilizing 3D forward and inversion procedures. We then assessed the reliability and resolution of optimum model based on sensitivitys test and a hypothetical inversion test (see **Methods**).

Result

The optimum model of 3D resistivity distribution reveals a conductive region (C1) and resistive region (R1) along the plate interface (Fig. 2). The C1 is located mainly within the subducting plate, where subducting seamounts are estimated to be situated[28]. We validated the C1 anomalies based on sensitivity tests which create replaced models in which the anomaly was filled with the resistivity value of the surrounding area (see **Methods**). The sensitivity test results indicated that the resistivity in C1 anomaly was less than 20 Ωm, with a deep limit extending beyond 70 km (Fig. 3a,b). On the other hand, heterogeneities within C1 are difficult to detected due to the resolution limitation of natural source marine MT data[36]. The R1 is mainly within the overriding Eurasian Plate at depths between 5 and 40 km (Fig. 2). Sensitivity test results indicated a resistivity greater than 430 Ωm in R1 (Fig. 3c). The hypothetical inversion test successfully reconstructs both the resistive and conductive anomalies in the expected locations (Supplementary Figs. S1, S2) (see **Methods**). However, the model shows poor recovery in the deep part of the conductive anomaly and obscured boundaries of both the anomalies due to the smoothness constraint and low sensitivity at greater depths, as demonstrated in the sensitivity test for the depth of C1 (Fig. 3b).

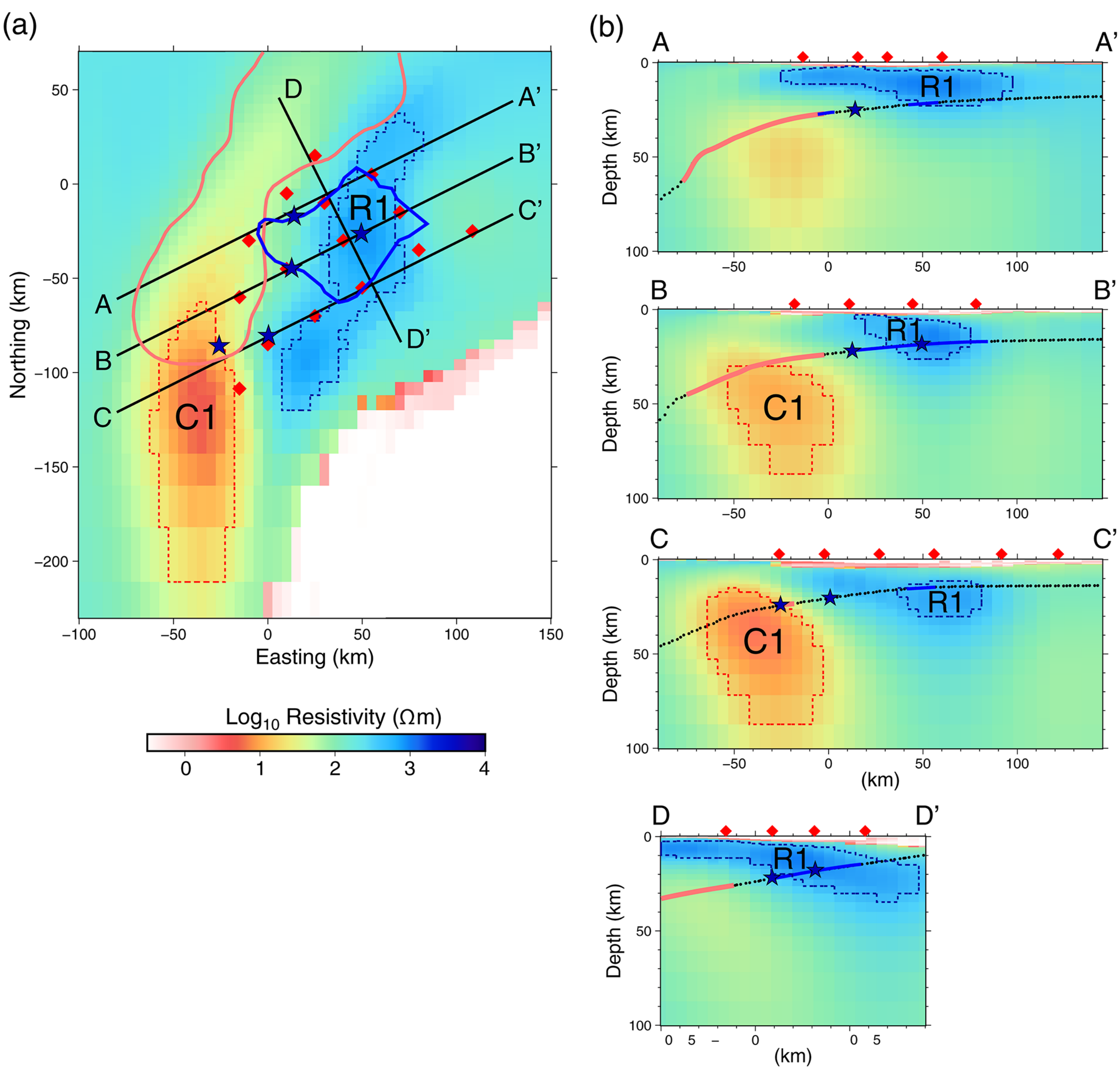

Fig. 2. 3D Resistivity model. Red diamonds indicate OBEM observation sites, and red and blue dashed lines enclose the areas used for the sensitivity tests of the C1 (19.03 Ωm) and R1 (430.6 Ωm) anomalies, respectively. (**a**) Resistivity section along the plate interface. (**b**) Vertical cross sections along lines A–A', B–B', C–C', and D–D' in (**a**). On each section, the black dotted line indicates the plate boundary interface[66]. Blue and pink solid lines denote the slip areas of regular earthquakes[25,68] and long-term SSEs[27], respectively. Blue stars represent regular earthquakes (M > 7.0) as determined by the Japan Meteorological Agency. Note that the vertical positions of the regular earthquakes in (**b**) are assumed to be on the plate interface due to the low accuracy of vertical location determination.

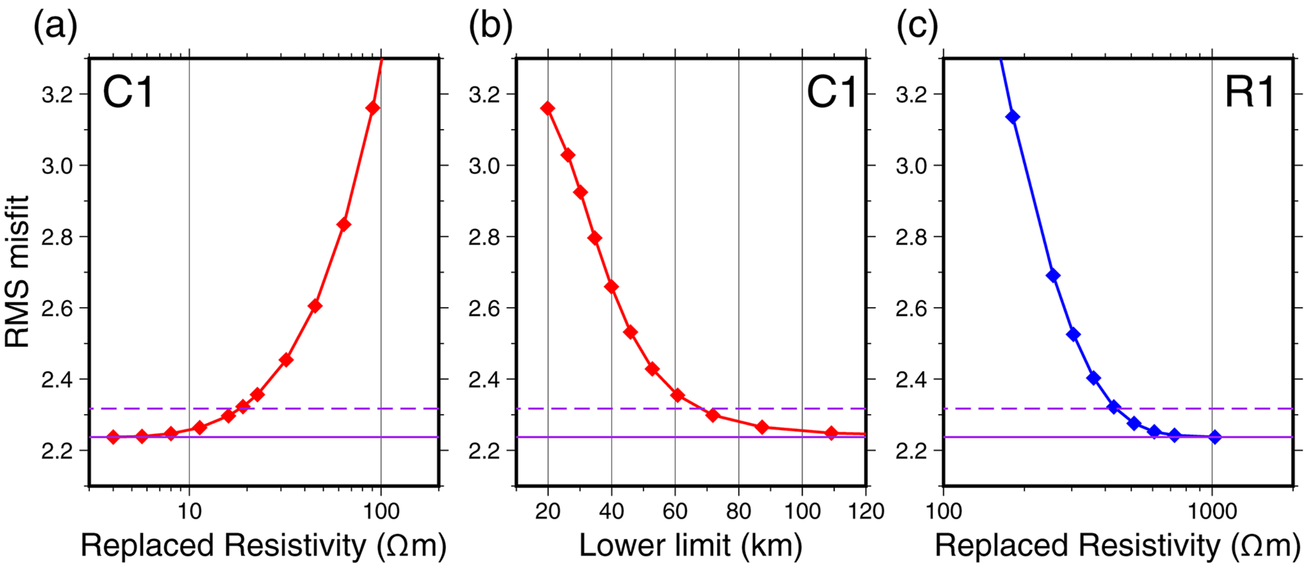

Fig. 3. RMS misfits of the sensitivity test models of the C1 and R1 anomalies. The solid and dashed purple lines indicate the RMS misfit of the optimum model and the 95% confidence limit (one-sided *F*-test), respectively.

Discussion

Hydrous subducting seamounts

We interpreted the main cause of C1 to be a high amount of saline fluid in interconnected pores that significantly reduced the bulk resistivity of the rock, as reported in other subduction zones[17,21]. In this area, the seismic tomographic surveys also show low seismic velocity anomalies, which are interpreted as pore fluids[37,38]. Around the plate interface in C1, a serpentinized area is implied by a high Poisson's ratio, detected by a seismic tomographic survey[38]. Serpentine is formed by the hydration of mantle material; thus, it requires a supply of aqueous fluid from a deeper area in the subducting slab. Its presence, therefore, supports the presence of aqueous fluid in the C1 area. Fluid-filled serpentine areas, in which bulk resistivity is reduced, are a known cause of conductive anomalies[39,40].

Other factors that can decrease resistivity include the presence of conductive ores or partial melting. However, conductive ores (such as clay minerals, graphite, sulfides, and magnetite) are unlikely to be stable in the lower oceanic crust and mantle at this depth[41]. Moreover, the estimated temperature in the C1 area, between 200 and 600 ℃[42], does not exceed the solidus temperature of igneous rocks such as granite, basalt[43], gabbro[44], and peridotite[45], even under water-saturated conditions.

Seismic investigations have captured the shape of the subducting KPR, which includes several seamounts, within the Philippine Sea Plate on the southwest side of Hyuga-nada[28,29]. Since this low-velocity region is approximately located within the fluid-rich conductive region (C1) (Fig. 4b)[29], the subducting KPR is inferred to contain large amounts of pore fluid. The presence of hydrous subducting seamount could be a general feature, as a similar interpretation is made based on low V_s and high Poisson's ratio anomalies around the subducting Joban seamount chain in the NE Japan arc[46]. In addition, the precise seismic velocity image near line C–C' implies the migration of aqueous fluid into the overriding plate from the subducting KPR[10]. The hydrous C1 area above the plate interface supports the existence of migrated fluid in the overriding plate (Fig. 4).

A marine MT study of the Philippine Sea Plate has shown the presence of a conductive region at 40–80 km depth that is consistent with the position of the incoming KPR[36]; thus, the KPR may capture fluid before it is subducted beneath the Eurasian plate. Along the Hikurangi subduction margin, large amounts of aqueous fluid are trapped within seamounts on the incoming plate[17]. Therefore, seamounts can incorporate fluids such as seawater before subduction more easily than ordinary oceanic crust. Because the many seamounts, including subducting seamounts, observed along the KPR collectively have a large volume, a huge amount of aqueous fluid is likely transported into the Earth's interior in the western Hyuga-nada area. On the other hand, the low V_p anomaly at depths greater than 80 km around the subducting KPR is interpreted as hot mantle material rising through a slab window in the subducting Philippine Sea plate[47]. Therefore, the deep region of C1 may be attributed to a high-temperature anomaly.

Dry plate interface

The main factors causing resistive anomalies (R1) at this depth are a lack of fluid, and a lack of fluid interconnections. On islands near the study area, the presence of exposed Tertiary granites, which are generally dry and show high resistivity[48] (Fig. 1), suggests that such plutonic rocks in the overriding plate are responsible for a lack of pore fluid, or a lack of interconnections around R1 (Fig. 4). The results of seismic studies[49,50] showing a high P-wave velocity zone in the overriding plate are consistent with the presence of dense plutonic rocks with low fluid content in R1, because the P-wave velocity in granite is generally larger than that in accretionary

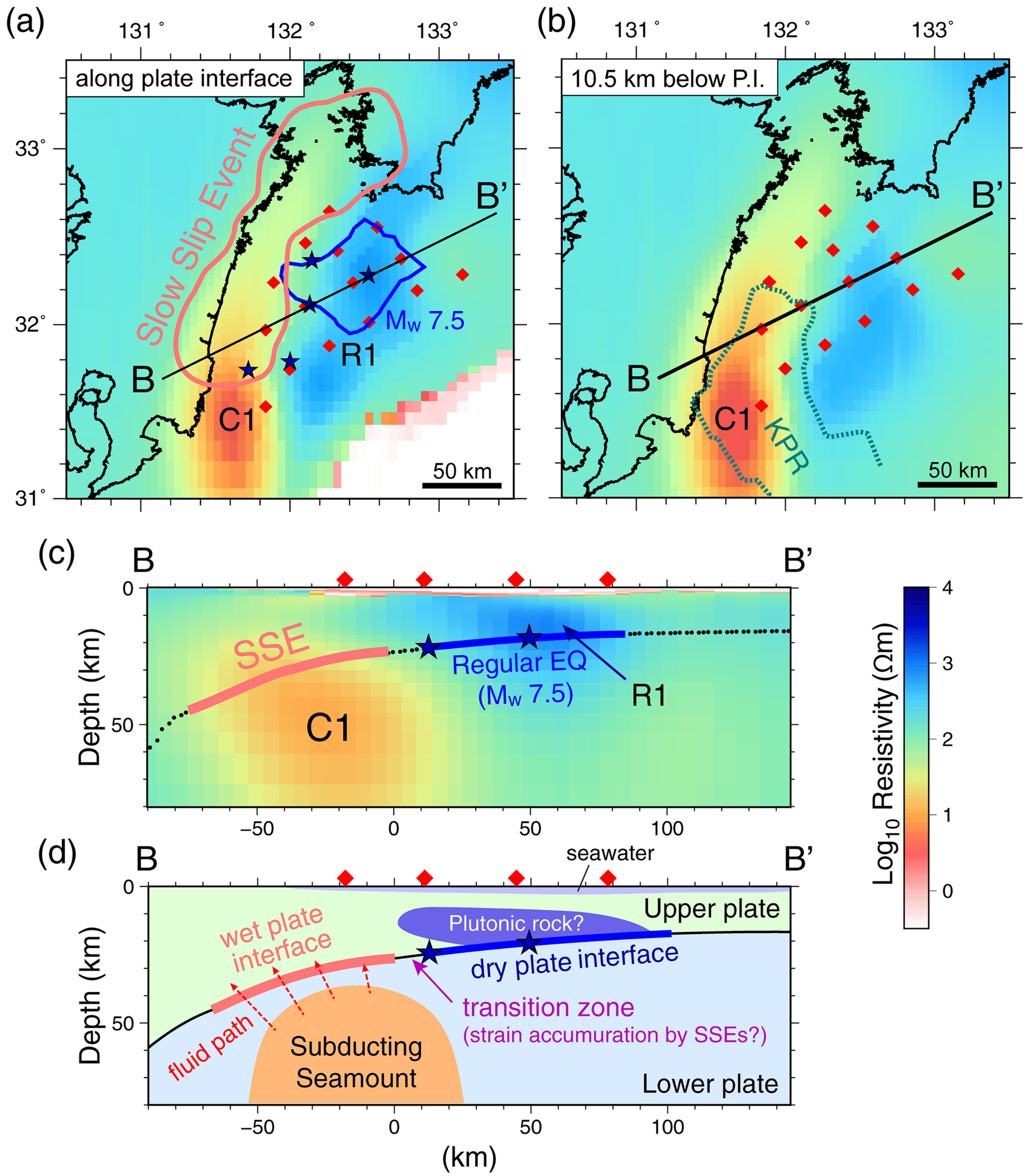

Fig. 4. (**a**) Resistivity section along the plate interface. (**b**) Resistivity section along a surface 10.5 km below the plate interface. Note that this surface corresponds to the region where KPR range was estimated based on low-velocity anomaly[29]. (**c**) Vertical section along line B–B'. (**d**) Interpretation of the section shown in (**c**). Red diamonds are OBEM observation sites. Other symbols are same as Fig. 2.

sedimentary rocks. Therefore, the most feasible interpretation of R1 is a lack of pore fluid or its interconnections due to the distribution of plutonic rock, although direct evidence is still needed to confirm the presence of plutonic rock in the R1 region.

Relationship between resistivity and earthquake distributions

Areas of long-term SSEs[27] are located around the upper part of the C1 conductive anomaly, which is interpreted as having a high amount of fluid derived from the subducting seamounts (see previous sub-section). Trapped pore fluid, which increases pore fluid pressure, has recently been discussed as a potential trigger to promote slow earthquakes[7,13]. In the south of C–C' profile, fluid migrated from the subducting KPR to the overriding plate is thought to enhance low-frequency tremors[10]. Off the Kii Peninsula in the Nankai Trough, structural change due to fluid migration are considered to precede very low-frequency earthquakes[51]. Although studies on the relationship between pore fluid and slow slip events are limited, fluid pressure fluctuations within the subducting oceanic crust are suggested to influence the timing of SSEs in the Hikurangi subduction zone[14]. Therefore, pore fluids derived from subducting seamounts likely enhance slow earthquakes activities, including SSEs, in the Hyuga-nada area. On the other hand, SSE has not been detected in the area of lowest resistivity within C1. Additionally, C1 has not been validated under the Bungo Channel, where the largest slip is estimated in the SSE region, although the model shows a slightly low resistivity anomaly (Fig. 2d).

Conversely, the R1 resistive region around the plate boundary interface, which indicates an area depleted of pore fluids, corresponds to the slip area of the largest Hyuga-nada earthquake in 1968 (M7.5)[25] (Fig. 4). Dry conditions along the plate interface can cause stick–slip behavior[15] and may have contributed to the fast fault slip during the 1968 event. The epicenters (rupture initiate points) of other large earthquakes (M7.1–7.2) are located in the transition zone between "dry" and "wet" areas (Fig. 4). The slip area of the 1968 earthquake is also in contact with the transition zone. For the M7-class earthquake regions in the intra-plate earthquake, epicenters area also located around the edge of the fluid rich area estimated based on resistivity, b-value and high Poisson's ratio[52–54].They may imply an effect of fluids initiating fast fault rupture.

Based on the above discussion, this study demonstrates a correlation between heterogeneous pore-fluid distribution and fault slip behavior in the Hyuga-nada region: SSEs occur in wet areas, whereas fast earthquakes originate in the transition zone to dry areas. A similar contrast in fluid distribution between slow and fast earthquakes has also been found in the Hikurangi margin[21], suggesting that this may be a general phenomenon. Because slow earthquakes have been suggested to contribute to strain transfer to adjacent fast earthquake zones[4,5], further investigations for detailed resistivity distribution and monitoring of resistivity changes are crucial. However, the hypothetical inversion test shows that the resolution of resistivity distribution is limited. To address these challenges, improving data quality is essential, particularly by increasing the density of observation points. In particular, for C1, which lies outside the observation network, integrating marine and land-based data is crucial. Additionally, it is important to incorporate seismologically and geologically verified plate boundaries into the resistivity inversion, allowing for resistivity discontinuities. Furthermore, establishing a probabilistic approach to quantify the reliability of model parameters[55] is necessary. These methodologies are not yet well established in three-dimensional resistivity structure analysis, making future advancements in these areas crucial challenges.

Methods

Marine magnetotelluric investigation

Magnetotelluric (MT) sounding, a passive exploration technique that employs natural electromagnetic variations, is used to identify deep resistivity heterogeneity. In this study, electromagnetic data were acquired at 15 observation sites on the seabed in the Hyuga-nada area (Fig. 1, Supplementary Table S1). The observations were conducted as a joint research project of Nagoya University, Kobe University, Kyoto University, University of Hyogo, and the Japan Agency for Marine-Earth Science and Technology (JAMSTEC). We deployed and recovered ocean bottom electro-magnetometers (OBEMs) during several research cruises conducted between March 2017 and September 2020 by training ship *Fukae-maru* (Kobe University) and research vessel *Kairei* (JAMSTEC). The OBEMs were deployed by free fall from the ship onto the seabed and were recovered via a self-pop-up system, in which the anchors are released by an acoustic signal from the ship. Observations were conducted by each OBEM for 5–12 months (Supplementary Table S1). For most of the observation period, measurements were made with a 60 s sampling interval to save power consumptions; for each OBEM, time series of electromagnetic field variations were obtained using a 0.125 s sampling interval over an approximately three-week period to estimate short-period MT impedances (less than several hundreds of seconds). Three orthogonal components of the magnetic field were measured with fluxgate magnetometers, two horizontal components of the electric field were measured with Ag–AgCl electrodes, and two components of tilt were measured for posture correction. Newly developed OBEMs equipped with an absolute pressure gauge were deployed at sites EMP1, EMP2, and NU9. At the other sites, conventional OBEM systems were deployed[56].

Estimation of magnetotelluric impedance

Magnetotelluric impedance (**Z**), which reflects the resistivity structure of the Earth, is obtained from the equation $\mathbf{E} = \mathbf{ZH}$, where **E** and **H** are the horizontal components of the electric and magnetic fields, respectively. At each site, **Z** was estimated from the observed electromagnetic field data as follows. First, the observed tilt data, the magnetic field data, and the IGRF-13 declination value[57] were used to apply posture corrections. The Bound Influence Remote Reference Processing code (BIRRP)[58] was then used to estimate MT impedances from the posture-corrected time series. To reduce the influence of local noise, magnetic field data at Kakioka Magnetic Observatory was used as a remote reference site[59,60]. Short-period (less than several hundreds of seconds) and long-period (more than several hundreds of seconds) MT impedances were estimated using the 1 s and 60 s sampled data, respectively. MT responses at NU2 and NU8, where magnetic field data were not available, were calculated using the electric field data at the site and the magnetic field data for NU3 and NU12, respectively.

High-quality MT impedances were estimated in a period range between 11 and 30,720 s (Fig. 5). The apparent resistivity and impedance phase obtained from the estimated short-period MT impedances indicate that the subsurface resistivity structure can be regarded as a 1D structure, because off-diagonal components of the impedance tensor were approximately equal and about one digit larger than diagonal components at most sites. The relatively low apparent resistivity in the short period range (less than 100 s) at most observation sites indicates the presence of a homogeneous conductive layer beneath the seafloor. The responses may exhibit distortions such as cusps of apparent resistivity, which are thought to be due to the effects of coastline and ocean topography[30,31] (e.g., around 300–3000 s at NU8, Fig. 5).

Construction of the initial resistivity model for inversion

Because derivation of the resistivity distribution from MT impedances is a nonlinear problem, resistivity models obtained by an inversion procedure depend on the initial model. This dependency is pronounced in the case of marine MT analyses, especially in coastal regions, because the observed response functions are strongly influenced by the bathymetry and the shape of the coastline[30]. Hence, we first used 3D forward modeling procedures to construct an appropriate initial model close to the actual structure. For the 3D forward and subsequent inversion analyses, we used a WSINV3DMT-based[61] 3D modeling code developed for marine MT impedance modeling that utilizes a staggered grid finite-difference method[35] to incorporate submarine topography. The mesh used for this analysis consisted of 79 × 79 × 61 (+ 9 air layers) blocks; it extended about 2200 km vertically and 4200 km × 4200 km horizontally (Supplementary Fig. S3). The horizontal mesh size was 5–8 km within the observation area and larger outside the observation area. The vertical mesh size was 100 m immediately beneath the sea surface and gradually increased with depth. The maximum size ratio of adjacent meshes was kept to 1.32 and 1.67 in the horizontal and vertical directions, respectively.

For the forward modeling, we constructed resistivity models consisting of seawater (0.3 Ωm), a conductive sediment layer beneath the seabed with uniform resistivity and uniform thickness, and an underlying background area with uniform resistivity. The bathymetry incorporated into these models was based on the ETOPO1 1-arc-minute global relief model[62] (Supplementary Fig. S3). The resistivity of the conductive layer was set to 1 Ωm by referring to the results of excavations in the Nankai trough off the Kii Peninsula[63]. The resistivity value of each block on the seafloor boundary was calculated by taking the volumetric average of the conductivity[35] based on the bathymetry. Because the conductive layer thickness and background resistivity were unknown, we varied these parameters between 0.1–8 km and 1–500 Ωm, respectively, and then determined the optimum model for each observation site by a grid search. For this modeling, we used 20 periods between 11 and 7,680 s to compute the impedance tensor. As an indicator of agreement between the data and the model response, we adopted the model with the minimum root mean square misfit (*RMSm*), which we calculated as follows:

$$RMSm\left(\mathbf{m}\right)=\sqrt{\frac{1}{N}\sum_{i=1}^{N}\frac{\left(d_i-f_i\left(\mathbf{m}\right)\right)^2}{\sigma_i^2}},$$

where d_i and $f_i\left(\mathbf{m}\right)$ are impedance components, observed and computed using model $\mathbf{m}$, respectively; σ_i is the estimated error of the observed impedance components; and *N* is the number of data (total of the real and imaginary parts of all impedance components at all sites). In this forward modeling and in the subsequent inversion procedures, the error floor was set to 3% of the sum of the squared impedance[64]. The *RMSm* distribution obtained by grid search indicates that the best-fit model differed among the observation sites (Supplementary Figs. S4, S5). First, the thickness of the 1 Ωm conductive subseafloor layer was greater in the south than in the north throughout the survey area (Supplementary Fig. S5a). This result implies that sediments just below the seabed were thicker on the south side. Second, the background resistivity with the lowest *RMSm* varied among the sites, and no spatial trend was apparent (Supplementary Fig. S5b). Third, the *RMSm* values of the models were small on the east side, but were large in the middle area (Supplementary Fig. S5c).

Using the forward modeling results, we constructed four three-layer models by using different background resistivities (50, 100, 200, and 500 Ωm) but otherwise the same parameter values (Supplementary Fig. S6). All of the models had a sub-seabed conductive layer with a thickness of 0.7 km in the north (around NU1, NU2, NU5, and EM4), 1 km in the middle north (NU3, NU7, NU8, NU11, NU12, and EM3), 2 km in the middle south (around EMP1, EMP2, and NU6), and 3 km in the south (around NU9 and NU10). The thickness of the conductive layer beneath shallow-water areas (water depth < 0.5 km) was set to 0.5 km because the sediment layer beneath the seafloor thins as it approaches land. Here, and also in the inversion analysis, we used impedances of 32–30,720 s. In total, $N = 2178$ data points were used for the calculations. MT responses computed from the forward models roughly matched the observed responses at the east and north stations; *RMSm* of the model with the minimum *RMSm* was 6.52 (background resistivity, 50 Ωm, Supplementary Fig. S7). However, improved models based on inversion analysis results are essential for explaining the observed responses, especially with regard to the following two points. First, the diagonal components of the forward model responses are about one order smaller than those of the observation data. Second, the model responses at around 100–1,000 s at sites NU1, EM3, EM4, and NU5 do not explain the cusps of apparent resistivity in the observed responses.

3D Inversion Analysis

Three-dimensional inversion analyses were performed using the four three-layer models described in the previous section as initial models. The inversion algorithm[35] estimates the optimum resistivity model by minimizing the following constrained objective function[61]:

$$W_\lambda\left(\mathbf{m}\right)=\left(\mathbf{m}-\mathbf{m}_p\right)^{\mathrm{T}}\mathbf{C}_m^{-1}\left(\mathbf{m}-\mathbf{m}_p\right)+\lambda^{-1}\left\{\left(\mathbf{d}-f\left[\mathbf{m}\right]\right)^{\mathrm{T}}\mathbf{C}_d^{-1}\left(\mathbf{d}-f\left[\mathbf{m}\right]\right)\right\},$$

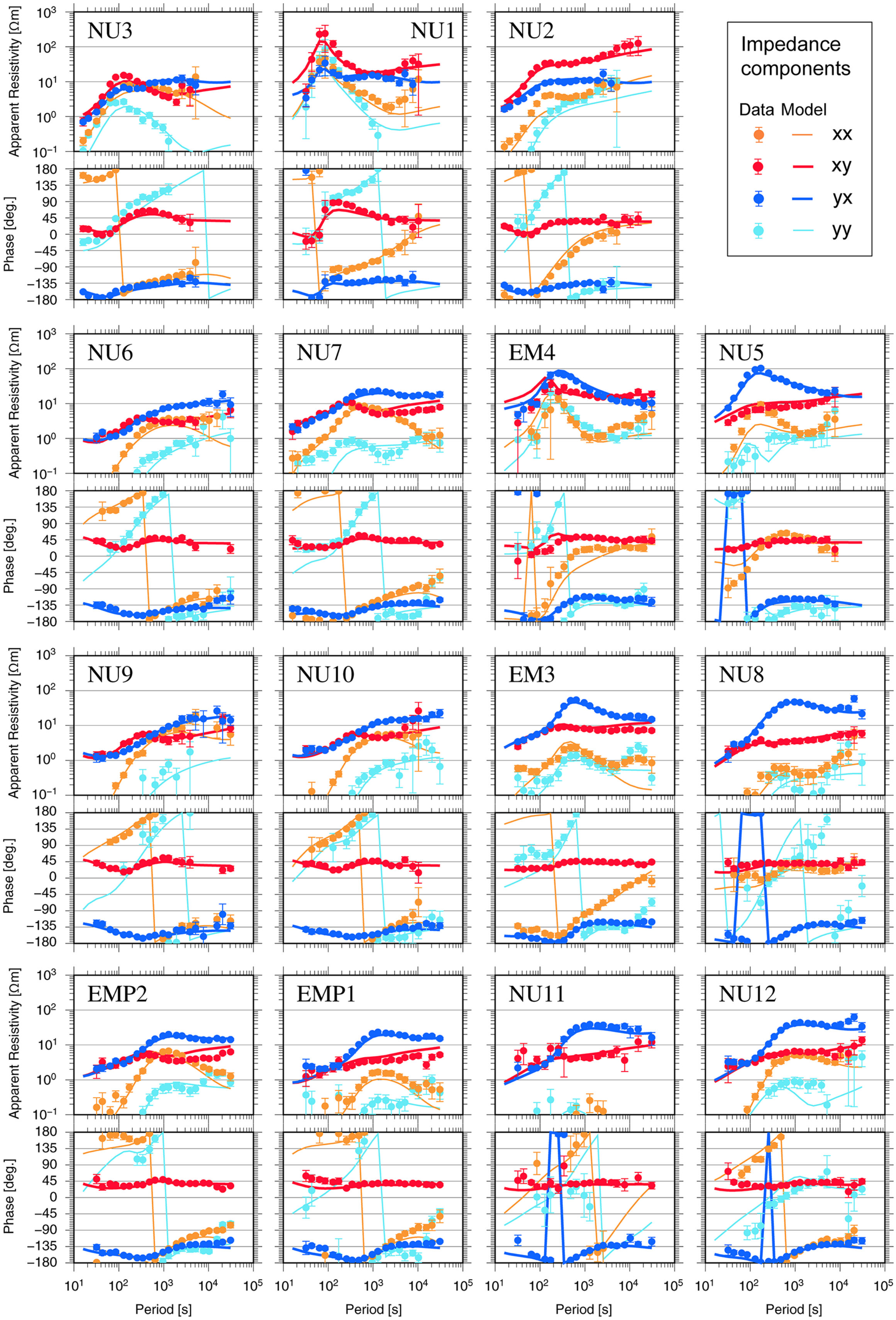

Fig. 5. Apparent resistivity and impedance phases of the observed and computed response functions for the optimum model.

where $\mathbf{m}_p$ is the prior model vectors; $\mathbf{d}$ is a data parameter vector consisting of the observed MT impedances; and $\mathbf{C}_m$ is the model covariance matrix, which characterizes the expected magnitude and smoothness of the resistivity variations relative to $\mathbf{m}_p$. $\mathbf{C}_d$ is a data covariance matrix representing the observation errors, and the superscript T represents the transpose. The term λ is a hyperparameter that balances the data misfit and model misfit terms, including model roughness; in the inversion procedure, it is determined by Occam's inversion approach[65].

The analyzed impedances ($\mathbf{d}$) were the same as the those used for the second stage of forward modeling. The calculation range and mesh size were the same as in the forward modeling. We attempted inversion procedures starting from the four initial models adopted in the second stage of forward modeling (background resistivity: 50, 100, 200, and 500 Ωm). The resistivity value for seawater was fixed at 0.3 Ωm during each iteration of the inversion analysis. In the first stage of inversion, the prior model ($\mathbf{m}_p$) was set to the same model as the initial one at the beginning of the inversion. The inversion procedure was iterated seven times. In the second stage of inversion, we adopted the initial and prior models from the best-fit model of the first stage inversion result and iterated the inversion procedures five times.

The resulting minimum *RMSm* model, which we adopted as the optimum model in this study, was derived from the initial model with a 200 Ωm background resistivity (*RMSm* = 2.23, Supplementary Fig. S8). Most model-predicted responses ($f\,[\mathbf{m}]$) matched the observed responses ($\mathbf{d}$), including those for the southwest stations and the diagonal components (Fig. 5), which were not adequately explained by the initial models. Additionally, cusps in apparent resistivity in the model responses at around 100–1000 s at sites NU1, EM3, EM4, and NU5, which were not explained in the forward modeling, were successfully reproduced in the inverted model. Because a large resistivity contrast between seawater and underground resistivity is required to explain coast effect[31], the resistive anomaly R1, situated near these OBEM sites, is essential to explain the observed cusp in apparent resistivity.

Sensitivity tests of resistivity anomalies

We validated the conductive anomaly C1 of the optimum model by creating replaced models in which the anomaly was filled with the resistivity value of the surrounding area; specifically, the area around C1 with resistivity higher than a threshold value was changed to that value. Forward analyses were performed by varying the threshold resistivity value between 4 and 128 Ωm. We then compared the *RMSm* of the optimum and replaced models (Fig. 3a). For quantitative evaluation, we adopted a one-sided *F*-test to determine whether the optimum and the replaced models were statistically different. The 95% confidence level of the *RMSm* obtained by *F*-test was 2.32 based on the optimum model *RMSm* (2.23) and the data quantity (2178). The obtained *RMSm* exceeded the criterion value (2.32) when the C1 was replaced with 19.03 Ωm. This result indicates that C1 had a resistivity of less than 20 Ωm.

The deep extension of C1 was also examined by filling the deeper region of C1, where resistivity was lower than 100 Ωm, with a resistivity value of 100 Ωm. Threshold depths were varied between 20 and 140 km. The calculated *RMSm* for the models indicated that if the lower boundary of the C1 anomaly was at a depth of less than approximately 70 km, the *F*-test criterion value was exceeded (Fig. 3b). Therefore, the C1 anomaly should extend to a depth greater than 70 km.

We also validated the resistive anomaly R1. Specifically, the resistive region around R1 with resistivity lower than a threshold value was replaced with that value. We varied the threshold value between 128 and 1024 Ωm. The calculated *RMSm* of the model showed that if the resistivity of the R1 anomaly was less than 430.6 Ωm, the *F*-test criterion value was exceeded (Fig. 3c). Therefore, the resistivity of the R1 anomaly was greater than 430 Ωm.

Hypothetical inversion test

We further assessed the reliability and resolution of the inverted resistivity model using a hypothetical inversion test, which inverts synthetic data generated from hypothetical resistivity model. The hypothetical model is based on the initial model of inversion (background resistivity: 200 Ωm) (Supplementary Fig. S6) but includes resistive (3000 Ωm) and conductive (1 Ωm) anomalies at locations corresponding to the R1 and C1 anomalies, respectively (Supplementary Fig. S1). We then calculated the model-predicted MT impedances (synthetic data) for this hypothetical model at the same locations and periods using the same forward modeling code[35] employed in the real data analyses. They synthetic data were assigned the same errors levels as those used in the inversion analyses. The same procedure applied to the real data was used for the hypothetical inversion test; however, to save computational costs, the inversion procedure was iterated four times in the first stage and two times in second stage. The RMSm (2.52 in the initial model) was reduced to 0.49 and 0.39 in the first second stages, respectively.

The hypothetical inversion successfully recovers both the resistive and conductive anomalies at the expected locations (Supplementary Fig. S2). The minimum resistivity in the conductive anomaly region is reduced to 7 Ωm (1 Ωm in the hypothetical model) from 200 Ωm in the initial model, despite the conductive anomaly being located out of the observation array. On the other hand, the model exhibits low recovery in the deep part in the conductive anomaly, consistent with the sensitivity test result for the depth of C1 (Fig. 3b), where RMSm changes are significantly reduced when lower depth limit of C1 is extended. The maximum resistivity in the resistive anomaly is increased to 1600 Ωm from 200 Ωm in the initial model, whereases the hypothetical value is 3000 Ωm.

Data availability

Data available on request form the primary corresponding author (Hiroshi Ichihara).

Received: 12 September 2024; Accepted: 6 May 2025
Published online: 16 May 2025

References

1. Hirose, H., Hirahara, K., Kimata, F., Fujii, N. & Miyazaki, S. A slow thrust slip event following the two 1996 Hyuganada earthquakes beneath the Bungo Channel, southwest Japan. *Geophys Res Lett* **26**, 3237–3240. https://doi.org/10.1029/1999gl010999 (1999).
2. Obara, K. Nonvolcanic deep tremor associated with subduction in southwest Japan. *Science* **296**, 1679–1681. https://doi.org/10.1126/science.1070378 (2002).
3. Nadeau, R. M. & Dolenc, D. Nonvolcanic tremors deep beneath the San Andreas Fault. *Science* **307**, 389–389. https://doi.org/10.1126/science.1107142 (2005).
4. Obara, K. Characteristic activities of slow earthquakes in Japan. *Proc. Jpn. Acad. Ser. B* **96**, 297–315. https://doi.org/10.2183/pjab.96.022 (2020).
5. Obara, K. & Kato, A. Connecting slow earthquakes to huge earthquakes. *Science* **353**, 253–257. https://doi.org/10.1126/science.aaf1512 (2016).
6. Kato, A. et al. Propagation of slow slip leading up to the 2011 M-w 9.0 Tohoku-Oki earthquake. *Science* **335**, 705–708. https://doi.org/10.1126/science.1215141 (2012).
7. Nishikawa, T., Ide, S. & Nishimura, T. A review on slow earthquakes in the Japan Trench. *Prog Earth Planet Sci* **10**. https://doi.org/10.1186/s40645-022-00528-w (2023).
8. Araki, E. et al. Recurring and triggered slow-slip events near the trench at the Nankai Trough subduction megathrust. *Science* **356**, 1157–1160. https://doi.org/10.1126/science.aan3120 (2017).
9. Plata-Martinez, R. et al. Shallow slow earthquakes to decipher future catastrophic earthquakes in the Guerrero seismic gap. *Nat Commun* **12**. https://doi.org/10.1038/s41467-021-24210-9 (2021).
10. Arai, R. et al. Upper-plate conduits linked to plate boundary that hosts slow earthquakes. *Nat. Commun.* **24**. https://doi.org/10.1038/s41467-023-40762-4 (2023).
11. Kodaira, S. et al. High pore fluid pressure may cause silent slip in the Nankai Trough. *Science* **304**, 1295–1298. https://doi.org/10.1126/science.1096535 (2004).
12. Shelly, D. R., Beroza, G. C., Ide, S. & Nakamula, S. Low-frequency earthquakes in Shikoku, Japan, and their relationship to episodic tremor and slip. *Nature* **442**, 188–191 (2006).
13. Takemura, S. et al. A review of shallow slow earthquakes along the Nankai Trough. *Earth Planets Space* **75**, 164. https://doi.org/10.1186/s40623-023-01920-6 (2023).
14. Warren-Smith, E. et al. Episodic stress and fluid pressure cycling in subducting oceanic crust during slow slip. *Nat. Geosci.* **12**, 475. https://doi.org/10.1038/s41561-019-0367-x (2019).
15. Scholz, C. H. *The Mechanics of Earthquakes and Faulting*. 3 edn, https://doi.org/10.1017/9781316681473 (Cambridge University Press, 2019).
16. Das, S. & Watts, A. B., Effect of subducting seafloor topography on the rupture characteristics of great subduction zone earthquakes. In: Lallemand, S., Funiciello, F. (eds) *Subduction Zone Geodynamics. Frontiers in Earth Sciences*. Springer, Berlin, 103–118. https://doi.org/10.1007/978-3-540-87974-9_6 (2009).
17. Chesley, C., Naif, S., Key, K. & Bassett, D. Fluid-rich subducting topography generates anomalous forearc porosity. *Nature* **595**, 255. https://doi.org/10.1038/s41586-021-03619-8 (2021).
18. Ichihara, H., Kasaya, T., Baba, K., Goto, T. & Yamano, M. 2D resistivity model around the rupture area of the 2011 Tohoku-oki earthquake (Mw 9.0). *Earth Planets Space* **75**. https://doi.org/10.1186/s40623-023-01828-1 (2023).
19. Naif, S., Key, K., Constable, S. & Evans, R. L. Porosity and fluid budget of a water-rich megathrust revealed with electromagnetic data at the Middle America Trench. *Geochem. Geophys. Geosyt.* **17**, 4495–4516. https://doi.org/10.1002/2016gc006556 (2016).
20. Heise, W. et al. Magnetotelluric imaging of fluid processes at the subduction interface of the Hikurangi margin. *New Zealand. Geophys. Res. Lett.* **39**, 55. https://doi.org/10.1029/2011gl050150 (2012).
21. Heise, W. et al. Electrical resistivity imaging of the inter-plate coupling transition at the Hikurangi subduction margin, New Zealand. *Earth Planet Sci. Lett.* **524**. https://doi.org/10.1016/j.epsl.2019.115710 (2019).
22. Heise, W. et al. Changes in electrical resistivity track changes in tectonic plate coupling. *Geophys Res Lett* **40**, 5029–5033. https://doi.org/10.1002/Grl.50959 (2013).
23. Heise, W. et al. Mapping subduction interface coupling using magnetotellurics: Hikurangi margin. *New Zealand. Geophys Res Lett* **44**, 9261–9266. https://doi.org/10.1002/2017gl074641 (2017).
24. Miyazaki, S. & Heki, K. Crustal velocity field of southwest Japan: Subduction and arc-arc collision. *J Geophys Res-Sol Ea* **106**, 4305–4326. https://doi.org/10.1029/2000jb900312 (2001).
25. Yagi, Y., Kikuchi, M., Yoshida, S. & Yamanaka, Y. Source Process of the Hyuga-nada Earthquake of April 1, 1968 (M_{JMA}7.5), and its Relationship to the Subsequent Seismicity. *Zisin (Journal of the Seismological Society of Japan. 2nd ser.)* **51**, 139–148. https://doi.org/10.4294/zisin1948.51.1_139 (1998).
26. Yamashita, Y. et al. Migrating tremor off southern Kyushu as evidence for slow slip of a shallow subduction interface. *Science* **348**, 676–679 (2015).
27. Takagi, R., Uchida, N. & Obara, K. Along-strike variation and migration of long-term slow slip events in the Western Nankai Subduction Zone, Japan. *J Geophys Res-Sol Earth* **124**, 3853–3880. https://doi.org/10.1029/2018jb016738 (2019).
28. Park, J. O., Hori, T. & Kaneda, Y. Seismotectonic implications of the Kyushu-Palau ridge subducting beneath the westernmost Nankai forearc. *Earth Planets Space* **61**, 1013–1018. https://doi.org/10.1186/Bf03352951 (2009).
29. Yamamoto, Y. et al. Imaging of the subducted Kyushu-Palau Ridge in the Hyuga-nada region, western Nankai Trough subduction zone. *Tectonophysics* **589**, 90–102. https://doi.org/10.1016/J.Tecto.2012.12.028 (2013).
30. Worzewski, T., Jegen, M. & Swidinsky, A. Approximations for the 2-D coast effect on marine magnetotelluric data. *Geophys J Int* **189**, 357–368. https://doi.org/10.1111/J.1365-246x.2012.05385.X (2012).
31. Key, K. & Constable, S. Coast effect distortion of marine magnetotelluric data: Insights from a pilot study offshore northeastern Japan. *Phys Earth Planet Interiors* **184**, 194–207. https://doi.org/10.1016/j.pepi.2010.11.008 (2011).
32. Wang, S. G., Constable, S., Reyes-Ortega, V. & Rychert, C. A. A newly distinguished marine magnetotelluric coast effect sensitive to the lithosphere-asthenosphere boundary. *Geophys J Int* **218**, 978–987. https://doi.org/10.1093/gji/ggz202 (2019).
33. Schwalenberg, K. & Edwards, R. N. The effect of seafloor topography on magnetotelluric fields: An analytical formulation confirmed with numerical results. *Geophys J Int* **159**, 607–621. https://doi.org/10.1111/j.1365-246X.2004.02280.x (2004).
34. Baba, K., Tada, N., Utada, H. & Siripunvaraporn, W. Practical incorporation of local and regional topography in three-dimensional inversion of deep ocean magnetotelluric data. *Geophys J Int* **194**, 348–361. https://doi.org/10.1093/Gji/Ggt115 (2013).
35. Tada, N., Baba, K., Siripunvaraporn, W., Uyeshima, M. & Utada, H. Approximate treatment of seafloor topographic effects in three-dimensional marine magnetotelluric inversion. *Earth Planets Space* **64**, 1005–1021. https://doi.org/10.5047/Eps.2012.04.005 (2012).
36. Tada, N., Baba, K. & Utada, H. Three-dimensional inversion of seafloor magnetotelluric data collected in the Philippine Sea and the western margin of the northwest Pacific Ocean. *Geochem Geophys Geosyst* **15**, 2895–2917. https://doi.org/10.1002/2014gc005421 (2014).

37. Wang, Z. & Zhao, D. P. Vp and Vs tomography of Kyushu, Japan: New insight into arc magmatism and forearc seismotectonics. *Phys Earth Planet Interiors* **157**, 269–285. https://doi.org/10.1016/j.pepi.2006.04.008 (2006).
38. Tahara, M. et al. Seismic velocity structure around the Hyuganada region, Southwest Japan, derived from seismic tomography using land and OBS data and its implications for interplate coupling and vertical crustal uplift. *Phys Earth Planet Interiors* **167**, 19–33. https://doi.org/10.1016/j.pepi.2008.02.001 (2008).
39. Ichihara, H. et al. Imaging of a serpentinite complex in the Kamuikotan Zone, northern Japan, from magnetotelluric soundings. *Earth Planets Space* **73**, 154. https://doi.org/10.1186/s40623-021-01482-5 (2021).
40. Ichihara, H., Mogi, T., Satoh, H. & Yamaya, Y. Electrical resistivity modeling around the Hidaka collision zone, northern Japan: regional structural background of the 2018 Hokkaido Eastern Iburi earthquake (M_w 6.6). *Earth Planets Space*, **71**, 100. https://doi.org/10.1186/s40623-019-1078-7 (2019).
41. Yang, X. Z. Origin of high electrical conductivity in the lower continental crust: A review. *Surv Geophys* **32**, 875–903. https://doi.org/10.1007/s10712-011-9145-z (2011).
42. Yoshioka, S. & Murakami, K. Temperature distribution of the upper surface of the subducted Philippine Sea Plate along the Nankai Trough, southwest Japan, from a three-dimensional subduction model: relation to large interplate and low-frequency earthquakes. *Geophys J Int* **171**, 302–315. https://doi.org/10.1111/j.1365-246X.2007.03510.x (2007).
43. Murphy, J. B. Igneous rock associations 7. Arc magmatism I: Relationship between subduction and magma genesis. *Geosci Can* **33**, 145–167 (2006).
44. Lambert, I. B. & Wyllie, P. J. Melting of Gabbro (Quartz Eclogite) with excess water to 35 kilobars, with geological applications. *J Geol* **80**, 693–700. https://doi.org/10.1086/627795 (1972).
45. Mysen, B. O. & Boettcher, A. L. Melting of a hydrous mantle.1. Phase relations of natural peridotite at high-pressures and temperatures with controlled activities of water, carbon-dioxide, and hydrogen. *J. Petrol.* **16**, 520–548 (1975).
46. Wang, Z. & Lin, J. Role of fluids and seamount subduction in interplate coupling and the mechanism of the 2021 Mw 7.1 Fukushima-Oki earthquake, Japan. *Earth Planet Sci. Lett.* **584**. https://doi.org/10.1016/j.epsl.2022.117439 (2022).
47. Cao, L. M., Wang, Z., Wu, S. G. & Gao, X. A new model of slab tear of the subducting Philippine Sea Plate associated with Kyushu-Palau Ridge subduction. *Tectonophysics* **636**, 158–169. https://doi.org/10.1016/j.tecto.2014.08.012 (2014).
48. Ichihara, H. *et al.* A 3D electrical resistivity model around the focal zone of the 2017 southern Nagano Prefecture earthquake (M_{JMA} 5.6): implications for relationship between seismicity and crustal heterogeneity. *Earth Planets Space* **70**. https://doi.org/10.1186/s40623-018-0950-1 (2018).
49. Yamamoto, Y. et al. Seismicity and structural heterogeneities around the western Nankai Trough subduction zone, southwestern Japan. *Earth Planet Sc Lett* **396**, 34–45. https://doi.org/10.1016/j.epsl.2014.04.006 (2014).
50. Nishizawa, A., Kaneda, K. & Oikawa, M. Seismic structure of the northern end of the Ryukyu Trench subduction zone, southeast of Kyushu, Japan. *Earth Planets Space* **61**, E37–E40. https://doi.org/10.1186/Bf03352942 (2009).
51. Tonegawa, T., Takemura, S., Yabe, S. & Yomogida, K. Fluid Migration Before and During Slow Earthquakes in the Shallow Nankai Subduction Zone. *J. Geophys. Res-Sol. Ea.* **127**. https://doi.org/10.1029/2021JB023583 (2022).
52. Aizawa, K. *et al.* Electrical conductive fluid-rich zones and their influence on the earthquake initiation, growth, and arrest processes: observations from the 2016 Kumamoto earthquake sequence, Kyushu Island, Japan. *Earth Planets Space* **73**, https://doi.org/10.1186/s40623-020-01340-w (2021).
53. Ichihara, H. et al. Crustal structure and fluid distribution beneath the southern part of the Hidaka collision zone revealed by 3-D electrical resistivity modeling. *Geochem Geophys Geosyst* **17**, 1480–1491. https://doi.org/10.1002/2015gc006222 (2016).
54. Singh, A. P., Mishra, O. P., Yadav, R. B. S. & Kumar, D. A new insight into crustal heterogeneity beneath the 2001 Bhuj earthquake region of Northwest India and its implications for rupture initiations. *J Asian Earth Sci* **48**, 31–42. https://doi.org/10.1016/j.jseaes.2011.12.020 (2012).
55. Ichihara, H., Kuwatani, T., Tada, N. & Nagata, K. Probabilistic estimation of model parameters through grid search approaches: applications to geomagnetic anomaly source estimations. *Earth Planets Space* **77**, 26. https://doi.org/10.1186/s40623-025-02141-9 (2025).
56. Kasaya, T. & Goto, T. A small ocean bottom electromagnetometer and ocean bottom electrometer system with an arm-folding mechanism. *Explor Geophys* **40**, 41–48. https://doi.org/10.1071/Eg08118 (2009).
57. Alken, P. *et al.* International geomagnetic reference field: the thirteenth generation. *Earth Planets Space* **73**. https://doi.org/10.1186/s40623-020-01288-x (2021).
58. Chave, A. D. & Thomson, D. J. Bounded influence magnetotelluric response function estimation. *Geophys J Int* **157**, 988–1006. https://doi.org/10.1111/J.1365-246x.2004.02203.X (2004).
59. Kakioka Magnetic Observatory. Kakioka geomagnetic field 1-second digital data in IAGA-2002 format, Kakioka Magnetic Observatory Digital Data Service, https://doi.org/10.48682/186bd.58000 (2013).
60. Gamble, T. D., Clarke, J. & Goubau, W. M. Magnetotellurics with a remote magnetic reference. *Geophysics* **44**, 53–68 (1979).
61. Siripunvaraporn, W., Egbert, G., Lenbury, Y. & Uyeshima, M. Three-dimensional magnetotelluric inversion: data-space method. *Phys Earth Planet Interiors* **150**, 3–14 (2005).
62. NOAA, National Geophysical Data Center, ETOPO1 1 Arc-Minute Global Relief Model, https://doi.org/10.7289/V5C8276M (2009).
63. Wu, H. Y. et al. Observed stress state for the IODP Site C0002 and implication to the stress field of the Nankai Trough subduction zone. *Tectonophysics* **765**, 1–10. https://doi.org/10.1016/j.tecto.2019.04.017 (2019).
64. Rung-Arunwan, T., Siripunvaraporn, W. & Utada, H. On the Berdichevsky average. *Phys Earth Planet Interiors* **253**, 1–4. https://doi.org/10.1016/j.pepi.2016.01.006 (2016).
65. Constable, S. C., Parker, R. L. & Constable, C. G. Occams inversion: A practical algorithm for generating smooth models from electromagnetic sounding data. *Geophysics* **52**, 289–300 (1987).
66. Iwasaki, T., Sato, H., Shinohara, M., Ishiyama, T. & Hashima, A. in *2015 Fall Meeting, American Geophysical Union*, San Francisco (2015).
67. Geological Survey of Japan. Seamless digital geological map of Japan V2 1: 200,000. https://gbank.gsj.jp/seamless (2022).
68. Sagiya, T. & Thatcher, W. Coseismic slip resolution along a plate boundary megathrust: The Nankai Trough, southwest Japan. *J Geophys Res-Sol Earth* **104**, 1111–1129. https://doi.org/10.1029/98jb02644 (1999).
69. Wessel, P. et al. The generic mapping tools version 6. *Geochem Geophy Geosy* **20**, 5556–5564. https://doi.org/10.1029/2019gc008515 (2019).
70. Lindquist, K. G., Engle, K., Stahlke, D. & Price, E. Global topography and bathymetry grid improves research efforts. *Eos Trans. AGU* **85**(19), 186 (2004).

Acknowledgements
We thank the captains and crews of Training Ship Fukae-maru (Kobe University) and Deep Sea Research Vessel Kairei (JAMSTEC), as well as the scientific party of each cruise, for deploying and retrieving the OBEMs. We thank Prof. Kimihiro Mochizuki from the University of Tokyo supported the observations. Thoughtful comments from three anonymous reviewers improved our manuscript. GMT software[69] was used to create the figures. The plate models were constructed from topography and bathymetry data provided by the Geospatial

Information Authority of Japan (250-m digital map), the Japan Oceanographic Data Center (500-m mesh bathymetry data, J-EGG500), and the Geographic Information Network of Alaska, University of Alaska[70]. This work was partly funded by JSPS KAKENHI grants (16H06475 "Science of Slow Earthquake" and 16K17793).

Author contributions

H.I., T.G., T.M., N.T., S.S., and H.N. contributed to the observations. H.N. and M.K. analyzed the data. H.N. and H.I. drafted the manuscript. All authors contributed to the interpretation of the data and approved the final manuscript.

Declarations

Competing interests

The authors declare no competing interests.

Additional information

Supplementary Information The online version contains supplementary material available at https://doi.org/10.1038/s41598-025-01440-1.

Correspondence and requests for materials should be addressed to H.I.

Reprints and permissions information is available at www.nature.com/reprints.

Publisher's note Springer Nature remains neutral with regard to jurisdictional claims in published maps and institutional affiliations.